catalysts

MDPI

*Article*

# Rapid and Efficient Removal of Rhodamine B by a Novel Nickel Oxide/Attapulgite Fenton-like Catalyst: Improved Adsorption and Fenton-like Oxidation

**Sadiq Ali [1], Saeed Ahmed [2,*], Huiyu Li [1] and Yongjun Feng [1,3,*]**

[1] State Key Laboratory of Chemical Resource Engineering, College of Chemistry, Beijing University of Chemical Technology, No. 15 Beisanhuan East Road, Chaoyang District, Beijing 100029, China; sadiqalibwp@outlook.com (S.A.); huiyuli@mail.buct.edu.cn (H.L.)
[2] Department of Biological & Chemical Sciences, University of Rasul, Mandi Bahauddin 50370, Pakistan
[3] Key Laboratory of Characteristic Mineral Functional Materials and Applications of XPCC, College of Chemistry and Chemical Engineering, Tarim University, Alar 843300, China
* Correspondence: saeed.ahmed@putrasul.edu.pk (S.A.); yjfeng@mail.buct.edu.cn (Y.F.)

## Abstract

A nickel oxide/attapulgite (A-ATP/NiO) nanocomposite was synthesized and evaluated for the adsorption and Fenton-like degradation of Rhodamine B (Rh-B) in an aqueous solution. The composite was characterized using X-ray diffraction (XRD), Fourier transform infrared spectroscopy (FTIR), scanning electron microscopy (SEM), energy dispersive X-ray spectroscopy (EDS), and Brunauer-Emmett-Teller (BET), confirming the successful immobilization of NiO nanoparticles into the attapulgite framework. The attapulgite modification results in enhanced surface properties, including increased surface area (from 68.9 to 111.3 $m^2\ g^{-1}$), pore volume, and the availability of active sites. Batch experiments demonstrated a high affinity of A-ATP/NiO toward Rh-B, achieving 52% adsorption within 60 min. Upon addition of Fenton reagent ($H_2O_2$), the composite exhibited excellent catalytic performance, achieving 97% Rh-B degradation in 10 min and almost complete removal (99.39%) within 60 min under optimized conditions (pH 3, 303 K, $H_2O_2$ 5 mmol $L^{-1}$, catalyst dose 0.03 g $L^{-1}$, dye concentration 50 ppm). The synergistic combination of adsorption and catalytic oxidation significantly enhanced dye removal, with reactive hydroxyl radicals (•OH) driving the degradation process. Kinetic analysis indicated that the removal followed a pseudo-first-order model, suggesting that physisorption and surface diffusion are the primary mechanisms for Rh-B degradation. These findings highlight A-ATP/NiO as a low-cost, environmentally friendly, and highly efficient material for the rapid and sustainable remediation of Rh-B-contaminated wastewater.

**Keywords:** adsorption; attapulgite clay; Fenton-like degradation; nickel oxide; Rhodamine B



Academic Editors: Jean-François Lamonier, Guoqiang Cao and Rafael Rodríguez Solís

Received: 15 May 2026
Revised: 24 June 2026
Accepted: 21 July 2026
Published: 29 July 2026



## 1. Introduction

Water pollution from synthetic dyes, predominantly used in textile, leather, plastics, printing, and paper industries, remains one of the most severe environmental threats of the present era [1]. These industries collectively consume enormous quantities of water while releasing substantial volumes of dye-laden effluents (up to 200 L per kg of textile processed), resulting in large amounts of wastewater (e.g., textile dyeing and printing sectors alone account for ~16.7% of industrial COD emissions) [2]. Each year, the global textile industry contributes to the production of over 70 million tons of synthetic dyes, a

significant portion of which, estimated between 10 and 50%, is discharged untreated into water bodies due to poor fixation efficiency, leading to widespread pollution of aquatic environments [3]. Chemical dyes in water bodies reduce light penetration, suppress photosynthesis in marine plants, drastically reduce dissolved oxygen, and disrupt the entire marine food chain [4]. These contaminants may bioaccumulate in organisms and enter the human food chain, posing serious risks such as skin diseases, respiratory ailments, organ toxicity, and carcinogenic effects [5].

To combat these hazards, multiple treatment strategies, such as adsorption, membrane filtration, biodegradation, advanced oxidation, and photocatalysis, have been explored. Among these, adsorption and heterogeneous Fenton-like advanced oxidation processes stand out for their cost-effectiveness, environmental compatibility, and ability to mineralize diverse organic pollutants in water [6]. The efficiency of these processes is predominantly influenced by the catalyst's nature and key operational parameters, including the initial pH of the solution, reaction time, catalyst amount, and concentrations of adsorbent and hydrogen peroxide ($H_2O_2$). To date, iron-based catalysts have been among the most widely employed in Fenton-like systems owing to their strong redox activity, affordability, and accessibility. Notably, iron oxide derived from the goethite phase has demonstrated effective degradation of methylene blue (MB). Similarly, iron-loaded attapulgite composites have demonstrated impressive catalytic performance in the removal of Rhodamine B (Rh-B), with degradation efficiencies exceeding 98%. In comparison, iron-doped biochar has also achieved Rh-B removal rates above 92.7% under optimal conditions [7].

Among available adsorbent materials, Attapulgite (ATP), a naturally abundant fibrous magnesium silicate clay, has gained attention as an adsorption matrix due to its high surface area, hierarchical microporous channels, and unique layered structure [8,9]. When functionalized with metal oxides, ATP-based composites synergistically combine pollutant adsorption with catalytic degradation of dyes such as methyl orange and Rhodamine B [10]. However, iron-based ATP composites can effectively remove dyes (e.g., >98% Rh-B removal). Still, they often face challenges, including reduced efficacy at low contaminant concentrations, iron leaching under acidic conditions, and sludge formation that complicates application and reuse [9]. To overcome these limitations, this work developed a nickel oxide-loaded attapulgite composite (ATP/NiO). Nickel oxide (NiO) offers robust Fenton-like oxidative potential with enhanced stability and lower metal dissolution compared to iron analogs. Preliminary studies indicate that NiO is effective for dye degradation. For example, green-synthesized NiO nanoparticles achieved up to 94% removal of Congo Red under optimized conditions, making it promising for industrial effluent treatment [11,12].

In this work, raw attapulgite (R-ATP) was first purified to yield purified attapulgite (P-ATP), which was then activated with an acid to produce acid-activated attapulgite (A-ATP) with increased compatibility and a larger surface area. A nickel oxide-loaded attapulgite A-ATP composite (A-ATP/NiO) was then fabricated and used for the degradation of Rh-B. Various experiments were conducted to investigate the effect of solution pH, temperature, catalyst dosage, contact time, and hydrogen peroxide concentration on the degradation performance. A kinetic study was also conducted to determine the reaction rate. Results confirm that A-ATP/NiO is an efficient, cost-effective, and eco-friendly catalyst for wastewater remediation.

## 2. Results and Discussion

### *2.1. Characterization of Catalysts*

#### 2.1.1. BET

The nitrogen ($N_2$) adsorption–desorption isotherms of R-ATP, P-ATP, P-ATP/NiO, and A-ATP/NiO were measured at 77 K (Figure 1a,b). All samples showed Type IV isotherms

with H3-type hysteresis according to the IUPAC classification [13]. The sharp rise in $N_2$ uptake at higher relative pressures ($P/P_o$) further confirms the presence of mesoporosity, which is essential for efficient mass transfer during adsorption and catalytic reactions. As summarized in Table 1, the textural properties vary considerably across the samples [14].

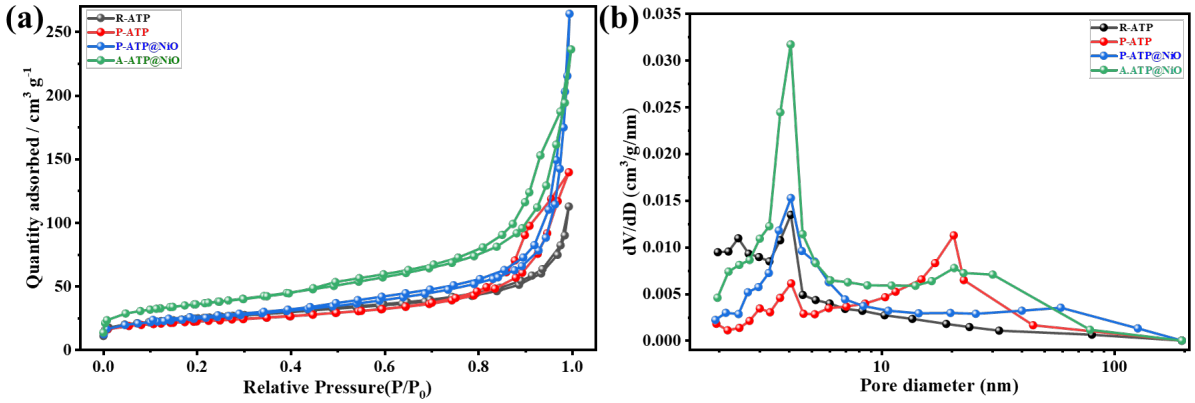


**Figure 1.** Nitrogen adsorption–desorption isotherms of (**a**) R-ATP, P-ATP, P-ATP/NiO, and A-ATP/NiO, and pore size distribution (**b**) R-ATP, P-ATP, P-ATP/NiO, and A-ATP/NiO.

**Table 1.** Results of BET analysis for R-ATP, P-ATP, P-ATP/NiO, and A-ATP/NiO.

| Samples | $S_{BET}$ ($m^2$ $g^{-1}$) | $V_t$ ($cm^3$ $g^{-1}$) | $d_p$ (nm) |
|---|---|---|---|
| R-ATP | 68.9 | 0.14 | 8.97 |
| P-ATP | 65.0 | 0.19 | 12.63 |
| P-ATP/NiO | 68.5 | 0.33 | 19.42 |
| A-ATP/NiO | 111.3 | 0.31 | 11.52 |

$S_{BET}$: specific surface area; $V_t$: total pore volume, and $d_p$: pore size.

The raw R-ATP and purified P-ATP possess surface areas of 68.9 $m^2/g$ and 65.0 $m^2/g$, respectively, with average pore diameters of 8.97 nm and 12.63 nm, as determined from BJH pore size distributions [15], indicating that purification alone modestly improves pore accessibility and removes surface impurities that could block adsorption sites. P-ATP/NiO showed a surface area of 68.5 $m^2/g$. Modification with NiO in P-ATP/NiO significantly increases the pore volume to 0.33 $cm^3/g$ and the average pore diameter to 19.42 nm, suggesting that NiO incorporation not only preserves the mesoporous network but also expands the accessible pore channels, facilitating better diffusion of target molecules. Remarkably, A-ATP/NiO exhibits the highest surface area of 111.3 $m^2/g$ and a pore volume of 0.31 $cm^3/g$ with an average pore diameter of 11.52 nm.

This substantial enhancement in surface area is attributed to the combined effects of purification, activation, and NiO modification, which expose additional active sites and prevent particle agglomeration. After purification, acid activation, and NiO incorporation, the increase in specific surface area, pore volume, and mesoporosity is now used to interpret the results. Previous studies reported that acid treatment removes mineral impurities, increases surface area, and enhances the mesoporous structure, thereby increasing pore accessibility [16]. Furthermore, acid activation creates functional groups on the surface, thereby improving the adsorption of $Ni^{2+}$ and the anchoring of NiO to the clay surface [17]. The NiO nanoparticles are also supported on attapulgite to suppress agglomeration and ensure uniform dispersion, thereby enhancing the number of catalytically active sites [18]. Thus, the better textural properties are well correlated with the adsorption capacity and catalytic degradation efficiency for Rh-B. The increase in mesoporosity and surface functionality directly correlates with the enhanced adsorption capacity and catalytic efficiency of

A-ATP/NiO, as larger surface areas and well-developed pores improve the accessibility of active sites for dye molecules and reactive radicals during Fenton-like degradation. Overall, the BET results demonstrate that strategic purification and NiO modification are critical for tailoring the textural properties of ATP-based nanocomposites, making A-ATP/NiO a highly promising candidate for the removal of organic pollutants through combined adsorption and catalytic oxidation.

#### 2.1.2. Functional Group Analysis

The FTIR spectra of R-ATP, P-ATP, A-ATP, P-ATP/NiO, and A-ATP/NiO in 4000–500 $cm^{-1}$ (Figure 2) illustrate the changes in functional groups in the nanocomposites. The extensive absorption band in the 3200–3600 $cm^{-1}$ of all samples is related to the stretching vibrations of surface -OH groups of the Al-OH and Mg-OH, and adsorbed moisture [19]. A small change in intensity after nanocomposite formation is due to hydrogen bonding and surface interactions between the metal oxides [20]. The weak bands at 2850–2950 $cm^{-1}$ in the C-H stretching vibrations are indicative of C-H stretching vibrations, which attest to the existence of organic moieties in ATP [21].

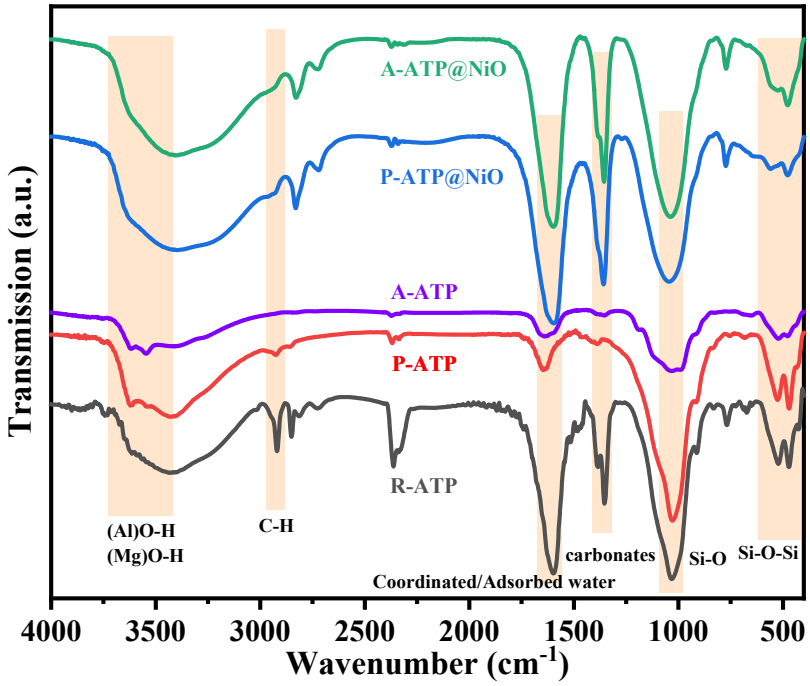


**Figure 2.** FTIR spectra of R-ATP, P-ATP, A-ATP, P-ATP/NiO, and A-ATP/NiO.

These C-H bands are observed in the R-APT and P-ATP. Still, they completely disappear in A-ATP and are not detected in the NiO-loaded samples (P-ATP/NiO and A-ATP/NiO), indicating that acid activation removes the organic surface species and that any residual organics do not persist after NiO incorporation [22]. The existence of a strong absorption within the range of 1600–1650 $cm^{-1}$ is attributed to coordinated or adsorbed water molecules, and also may be due to the bending vibrations of -OH groups. In the NiO-loaded samples (P-ATP/NiO and A-ATP/NiO), this band is more pronounced and slightly shifted, which proves good interaction between NiO nanoparticles and hydroxyl or water molecules on the surface, which facilitates the successful anchoring of NiO on the ATP matrix.

Compared with R-ATP, the absorption bands in the 1350–1500 $cm^{-1}$ region, particularly the band around 1465 $cm^{-1}$, are attributed to naturally occurring carbonate impurities in the raw attapulgite clay. The reduction or disappearance of these bands in P-ATP and

A-ATP indicates the partial removal of carbonate impurities during purification and acid activation with HCl. After NiO incorporation and calcination, changes in band intensity may be associated with NiO deposition on the ATP surface and with structural changes during thermal treatment. The presence of a strong absorption band in the range of 900–1100 $cm^{-1}$ is considered to have Si-O vibrations, which are the typical features of the ATP silicate structure [23]. Moreover, the intense peaks, with the maximum at approximately 1000–1100 $cm^{-1}$, correspond to Si-O-Si vibrations, indicating the structural integrity of the ATP clay. These bands do not disappear in response to modification and NiO loading, meaning that the silicate backbone does not disappear during synthesis [24].

#### 2.1.3. X-Ray Diffraction

The X-ray diffraction (XRD) of five samples, namely raw attapulgite (R-ATP), purified attapulgite (P-ATP), A-ATP, NiO-loaded attapulgite composite (P-ATP/NiO), and (A-ATP/NiO), is shown in Figure 3a. The peaks in the diffraction pattern labeled with dashed lines are the characteristic reflections of attapulgite, as per the JCPDS standard (PDF # 31-0783). These dominant peaks, including (110), (040), (−221), and (061), are observed in R-ATP, P-ATP, and A-ATP, indicating that the attapulgite structure is preserved during purification and acid activation. The diffraction peaks at 2θ = 37.2° as the (111), 43.3° as the (200), and 62.9° as the (220) crystallographic plane of NiO, which is indicative of the successful formation of the NiO phase within the composite [25].

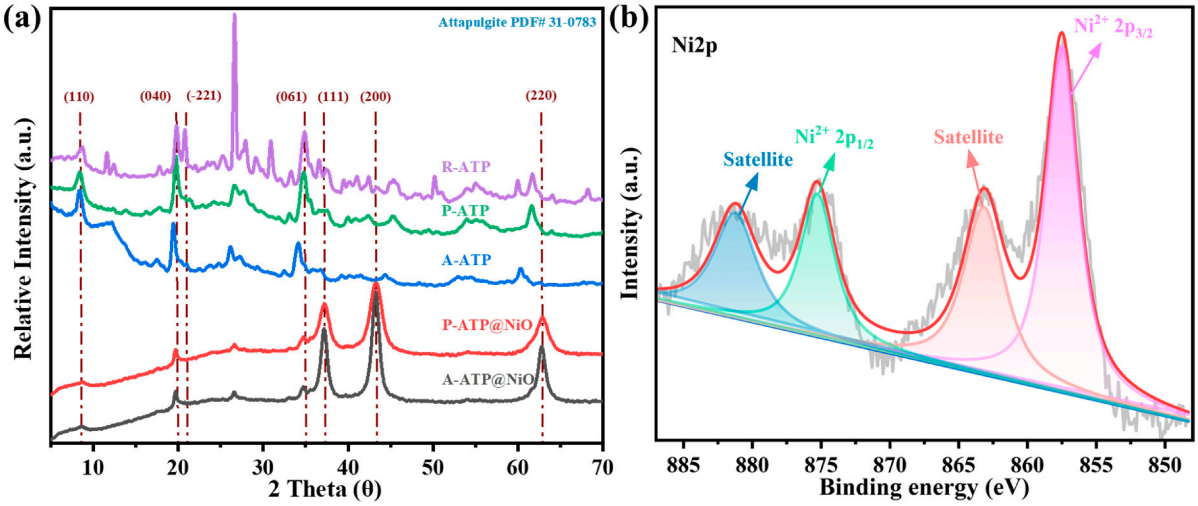


**Figure 3.** (**a**) XRD patterns of R-ATP, P-ATP, A-ATP, P-ATP/NiO, and A-ATP/NiO. (**b**) High-resolution XPS spectra of Ni2p of A-ATP/NiO showing $Ni^{2+}$ species and satellite peaks.

The P-ATP peaks are sharper and slightly stronger than those of R-ATP, indicating that the purification process also removes impurities and enhances crystallinity. At the same time, the A-ATP pattern shows the characteristic ATP reflections with slight intensity changes, confirming that activation preserves the main crystalline structure. Once NiO is deposited on the surface of attapulgite (P-ATP/NiO) and A-ATP/NiO, the pattern of diffusion is also changed significantly [26]. The attapulgite characteristic peaks are broadened and less intense, indicating that NiO particles partially cover ATP surfaces or that the composite formation reduces ATP crystallinity. The presence of these additional NiO-related diffraction peaks further confirms the successful incorporation of NiO into the attapulgite matrix.

The occurrence and intensity of these NiO peaks demonstrate that NiO is well dispersed on the ATP surface [27]. The peaks in the composite are broader than in pure NiO and are similar to those of the NiO particles, indicating a reduction in crystal size. As reported in the literature, at low Ni contents, the diffraction patterns of highly dispersed NiO phases on attapulgite may not show distinct peaks [18,28]. In contrast, the diffraction peaks at about 37.2°, 43.3°, and 62.9° are clearly visible and are attributed to the (111), (200), and (220) planes of NiO, respectively, thus confirming the existence of the NiO phase. In general, the XRD comparison illustrates three key aspects: (1) the structural framework of attapulgite remains intact after purification; (2) NiO is successfully incorporated into the ATP surface; (3) peak broadening and signal modification of the formed P-ATP/NiO or A-ATP/NiO composite are the outcomes of a high level of interaction between ATP and NiO. This validates the successful production of the composite material, in which both components are present and influence each other and their structures [29]. In Figure 3b, the XPS analysis further confirms that the high-resolution Ni 2p spectrum shows two main peaks at approximately 856.8–857.2 eV and 875.0–875.6 eV, corresponding to $Ni^{2+}$ $2p_{3/2}$ and $Ni^{2+}$ $2p_{1/2}$, respectively. In addition, two shake-up satellite peaks appear at 863.0–864.0 eV and 880.5–881.5 eV, characteristic of $Ni^{2+}$ in NiO. Therefore, the XPS results provide strong evidence for the successful presence of NiO in the catalyst [30].

#### 2.1.4. Scanning Electron Microscopy

The SEM images in Figure 4 show the morphological variations in attapulgite: raw (R-ATP), purified (P-ATP), loaded with NiO (P-ATP/NiO), and activated (A-ATP/NiO). In the crude ATP sample (Figure 4a), the typical rod-like fibrous structure of attapulgite is well observed, with elongated nanorods embedded in irregular plate-like shapes [31]. This building is indicative of the natural, raw clay that contains impurities and bundled structures. The P-ATP surface is purified (Figure 4b) with an evenly distributed structure. Fibrous rods become more unique and distinct, which means that the surface impurities and non-clay minerals have been removed [32]. The purified ATP sample shows more visible rod-like fibers and fewer non-fibrous surface deposits, as reported in previous work [31], which attributed the presence of mineral impurities associated with ATP, as well as partial separation of fiber bundles.

Upon NiO incorporation, the composite surface becomes rougher, with granular features, which are attributed to the attachment of NiO to the ATP fibers [33]. There are apparent morphological variations in the P-ATP/NiO composite (Figure 4c), resulting from the addition of the NiO nanoparticles onto the ATP surface. The smooth fibrous texture becomes coarser and more compact, and clusters of it can be seen, indicating that NiO is deposited on the ATP rods [34]. The granular structure in some areas indicates that NiO nanoparticles are densely attached to the ATP structure, partially covering its surface and altering its overall texture. An even more agglomerated and porous morphology is observed in the activated ATP loaded with NiO (A-ATP/NiO) in (Figure 4d). The fibers are interwoven and, to some extent, collapsed, forming an extremely irregular and rough surface [16]. This structural change suggests that activation enhanced the surface porosity and reactivity, with NiO deposition further roughening the surface. This modification is useful in adsorption applications because the structure provides more active sites and a larger surface area [35]. However, evidence of purification and surface area enhancement obtained from SEM is insufficient; therefore, EDX, FTIR, and BET analysis have been used to supplement the discussion.

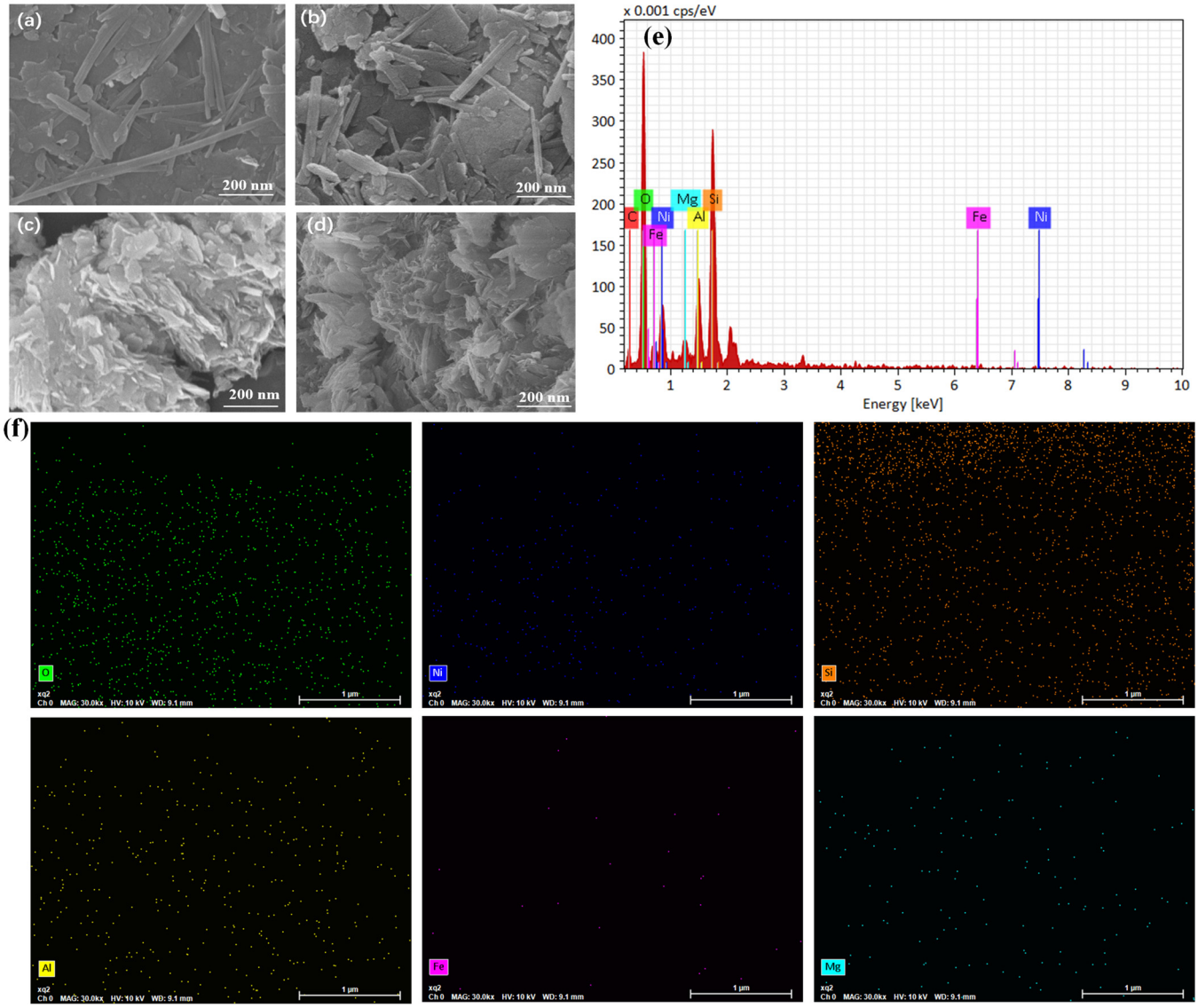


**Figure 4.** SEM images of (**a**) R-ATP, (**b**) P-ATP, (**c**) P-ATP/NiO, and (**d**) A-ATP/NiO, and EDX mapping of composite (**e**,**f**) A-ATP/NiO.

EDX elemental mapping confirms that Ni, the primary element, along with O, Si, Al, Fe, and Mg, has been successfully incorporated into the A-ATP/NiO nanocomposite and is homogeneously distributed, as illustrated in (Figure 4e,f). The percentage composition of each element is given in Table 2. It can be observed that oxygen (O) and silicon (Si) are not concentrated in any specific region but are distributed evenly throughout the structure. This is reasonable, since attapulgite clay is mainly composed of hydrated magnesium aluminum silicates. The strong, uniformly distributed Si and O signal indicates that the basic ATP structure remains intact following activation and NiO loading [36].

Moreover, the presence of aluminum (Al) and magnesium (Mg) throughout the sample further supports the notion that the structural components of ATP are retained within the composite. The distribution of nickel (Ni) is clearly evident with many bright, uniformly distributed spots in the Ni mapping [37]. It shows that NiO nanoparticles are deposited and well dispersed on the ATP surface, rather than forming large aggregates. A uniform distribution of Ni throughout the composite is desirable for improving catalytic and adsorptive properties, as it increases the number of active sites. Although at lower concentrations, iron (Fe) is also distributed throughout the material and may be contributed

by the mineral impurities or the activation process [38]. The overlay image of all the elements, namely O, Si, C, Al, Ni, Fe, and Mg, reflects their concurrent distribution in the composite structure. This uniformity shows strong interaction between ATP and NiO, facilitating efficient incorporation of NiO into the attapulgite framework under controlled conditions [18]. The major components are oxygen (42.22 wt%), silicon (26.48 wt%), and nickel (12.46 wt%), whereas Al, Mg, C, and Fe are present in smaller quantities. The Ni detection at a high weight percentage further indicates that the NiO-modified ATP composite was successfully formed.

**Table 2.** EDX Mapping of Nanocomposite A-ATP/NiO.

| Element | Atomic Number | Element Comp % | Atomic Comp % |
|---|---|---|---|
| O | 8 | 42.22 | 57.11 |
| Si | 14 | 26.48 | 20.40 |
| C | 6 | 5.14 | 9.26 |
| Al | 13 | 6.17 | 4.95 |
| Ni | 28 | 12.46 | 4.59 |
| Fe | 26 | 6.03 | 2.34 |
| Mg | 12 | 1.52 | 1.35 |

### *2.2. Degradation of Rhodamine B Dye*

#### 2.2.1. Effect of Catalysts on the Degradation of Rh-B

Figure 5 presents the removal behavior of Rh-B using five different catalysts: R-ATP, P-ATP, A-ATP, P-ATP/NiO, and A-ATP/NiO in two phases: the initial stage is adsorption, and the second stage is degradation after the addition of $H_2O_2$. The initial section of the graph (marked green) indicates the adsorption performance of the samples in the absence of an oxidizing agent [39]. In this case, A-ATP/NiO and P-ATP/NiO exhibit the highest adsorption of 52% and 49%, respectively, within 60 min, due to their sharp initial increases in removal rate. They have greater porosity and surface area, allowing more pollutant molecules to be captured. In contrast, A-ATP shows much higher adsorption (approximately 22%), P-ATP shows a relatively low adsorption efficiency (approximately 17%), and R-ATP shows the lowest adsorption efficiency (8%), consistent with its lower surface area and pore volume. The addition of $H_2O_2$ shifts the system from simple adsorption to Fenton-catalyzed degradation [40]. The second stage is characterized by a radical increase in Rh-B removal across all NiO-modified samples. However, A-ATP/NiO attains the highest degradation efficiency of almost 97% within 10 min and 99.39% within 60 min. The catalytic activity of the Fenton reaction, enhanced by the addition of NiO, significantly enhances the decomposition of $H_2O_2$ and the formation of reactive species that degrade Rh-B dye. P-ATP/NiO also shows good catalytic activity, achieving a degradation efficiency of nearly 97%, though its activity is slightly lower than that of A-ATP/NiO.

However, the degradation performance should not be evaluated solely by the absolute increase in removal percentage between 60 and 120 min, because the amount of Rh-B remaining after the adsorption stage varied across catalysts. P-ATP/NiO and A-ATP/NiO had already removed approximately 49% and 52% of Rh-B during adsorption; therefore, only about 51% and 48% of Rh-B remained available for Fenton-like degradation after $H_2O_2$ addition. In contrast, R-ATP removed only about 8% of Rh-B during adsorption, leaving about 92% in solution. Thus, the lower ΔRP% observed for P-ATP/NiO and A-ATP/NiO does not indicate weaker catalytic activity but mainly reflects their higher adsorption contribution before $H_2O_2$ addition. To compare the actual degradation of the

remaining Rh-B, the adsorption-corrected degradation efficiency was calculated using this Equation (1).

$$\text{Corrected degradation efficiency (\%)} = [(RP_t - RP_{60})/(100 - RP_{60})] \times 100 \quad (1)$$

where $RP_{60}$ is the removal percentage after adsorption, and $RP_t$ is the total removal percentage after the Fenton-like reaction. The corrected degradation efficiencies were approximately 85%, 94%, 95%, 98%, and 99% for R-ATP, P-ATP, A-ATP, P-ATP/NiO, and A-ATP/NiO, respectively, confirming the superior catalytic degradation performance of the NiO-modified samples. The degradation of the dye is very fast during the first 10 min (97%), which can be explained by the high percentage of active sites on A-ATP/NiO, the high activity of the $H_2O_2$, and the very quick formation of active oxygen species (•OH and $O_2^-$•) at high initial dye concentration. The degradation efficiency between 10 and 60 min is lower, which could be attributed to the significant decrease in Rh-B concentration, the limited likelihood of dye molecules and catalytic sites interacting, and the progressive approach to reaction equilibrium. In addition, other intermediate degradation products could temporarily bind to the active site and compete with the remaining dye molecules, thereby decreasing the reaction rate. This is a typical behavior observed in heterogeneous Fenton-like systems, which can be attributed to a shift from fast degradation to near-complete degradation, rather than to catalyst deactivation [41]. At the same time, compared with R-ATP, both P-ATP and A-ATP showed improved degradation efficiencies upon addition of $H_2O_2$, which indicates that purification and acid activation enhanced the catalytic activity of attapulgite. These results indicate that attapulgite without NiO can still activate $H_2O_2$ to some extent, likely due to the presence of intrinsic iron species in the clay structure. However, incorporating NiO significantly enhances both adsorption capacity and catalytic degradation efficiency by providing additional active sites for $H_2O_2$ activation and the generation of reactive oxygen species [42].

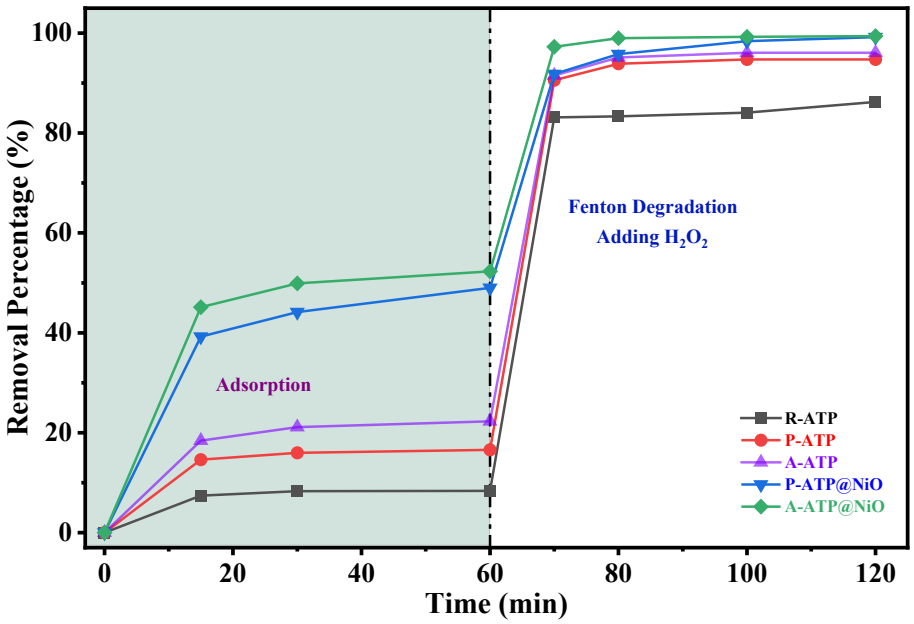


**Figure 5.** Effect of different catalysts (R-ATP, P-ATP, A-ATP, P-ATP/NiO, and A-ATP/NiO) on the degradation of Rh-B. Conditions [Rh-B] = 50 mg $L^{-1}$, [$H_2O_2$] = 5 mmol $L^{-1}$, catalyst dose = 0.03 g $L^{-1}$, pH = 3, T = 303 K.

2.2.2. Effect of Temperature on the Degradation of Rh-B

Figure 6 shows the influence of temperature on the Rh-B removal efficiency using A-ATP/NiO nanocomposite at two stages: the adsorption stage and the Fenton degradation stage after introducing $H_2O_2$. During the adsorption phase (marked in green), all four temperatures (303 K, 313 K, 323 K, and 333 K) exhibit the same trend, where the removal efficiency gradually increases over time. At 303 K, the adsorption reaches 52%. At the same time, the other temperatures show comparable behavior, indicating that the initial adsorption performance of the nanocomposite is only weakly dependent on temperature within the investigated range [43].

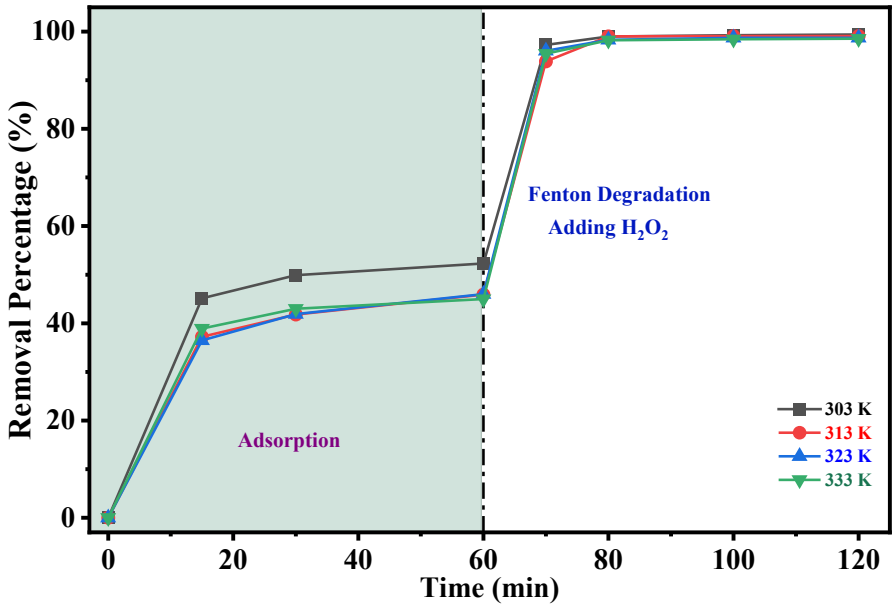


**Figure 6.** Effect of temperature on Rh-B degradation using A-ATP/NiO nanocomposite.

However, the slightly higher adsorption observed at 303 K suggests a minor variation in adsorption behavior under the tested conditions. Overall, the differences among these temperatures remain small, indicating that the adsorption performance of this material is not highly temperature-sensitive [44]. The system enters the Fenton degradation phase upon addition of $H_2O_2$, and the removal efficiency increases sharply at all temperatures, with Rh-B degradation reaching 99.39% [45]. This indicates that temperature has only a limited influence on the initial adsorption stage; the Fenton reaction proceeds rapidly and effectively across the tested temperature range. The results confirm that temperature has only a limited influence on Rh-B removal under the studied conditions. The approximately 50% removal observed before $H_2O_2$ addition mainly represents the adsorption contribution of A-ATP/NiO, not its catalytic degradation efficiency. After $H_2O_2$ addition, the remaining Rh-B was rapidly degraded, and nearly complete removal was achieved at all tested temperatures, confirming the effective Fenton-like catalytic activity of A-ATP/NiO.

2.2.3. Effect of Catalyst Dose

Figure 7 shows the removal efficiency of Rh-B over time during two consecutive treatment processes, i.e., adsorption and Fenton degradation. The catalyst (A-ATP/NiO) dosage is compared across three doses: 0.03 g $L^{-1}$, 0.02 g $L^{-1}$, and 0.01 g $L^{-1}$, corresponding to three different curves [46]. During the adsorption step (the first part of the graph, marked accordingly), there is a sudden, rapid increase in the removal efficiency at all three dosages [47]. Because there are many active sites on the catalyst surface, the removal efficiency increases rapidly during the adsorption phase at all tested doses.

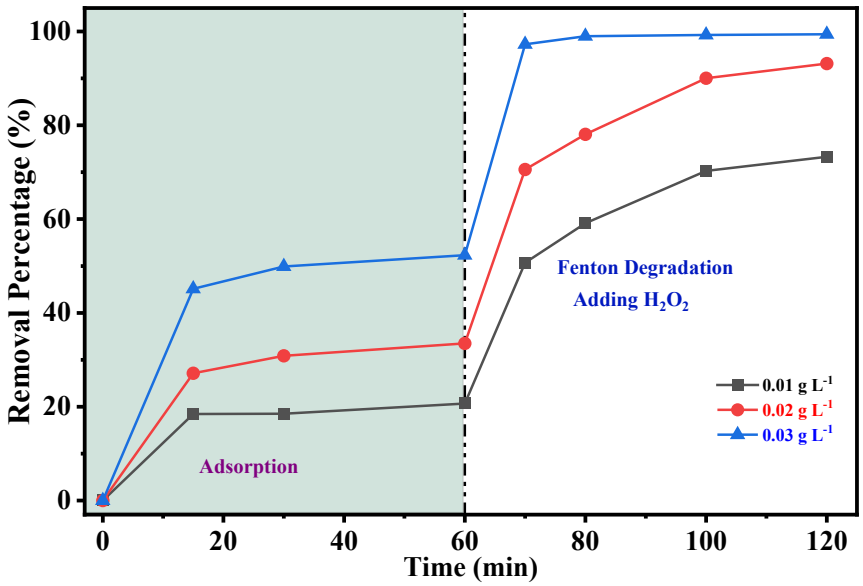


**Figure 7.** Influence of adsorbent dosage on the removal efficiency of Rh-B using A-ATP/NiO.

The removal efficiencies after 60 min are 20% for 0.01 g $L^{-1}$, 33% for 0.02 g $L^{-1}$, and 52% for 0.03 g $L^{-1}$, demonstrating clearly that higher catalyst doses provide more surface area and active sites, which promote adsorption [48]. Once the adsorption period is complete, $H_2O_2$ is introduced to trigger the Fenton reaction, resulting in a sudden increase in Rh-B removal efficiency across all doses. This abrupt rise indicates a shift from simple surface adsorption to catalytic degradation by hydroxyl radicals.

The increase in removal efficiency is most pronounced at the 0.03 g $L^{-1}$ dosage, which rapidly reaches almost complete removal (99.39%). The 0.02 g $L^{-1}$ dosage also shows a significant increase, reaching 93%, while the 0.01 g $L^{-1}$ dosage reaches 73%, both following slightly different gradients. Although the absolute ΔRP% between 60 and 120 min appears comparable and is slightly higher at 0.02 g $L^{-1}$, this comparison is influenced by differences in adsorption contributions before $H_2O_2$ addition. At 0.03 g $L^{-1}$, nearly 52% of Rh-B was already removed during adsorption, leaving less dye available for subsequent Fenton-like degradation. Therefore, the lower apparent ΔRP% at this dosage does not indicate weaker catalytic performance. Considering both adsorption and degradation of the remaining Rh-B, 0.03 g $L^{-1}$ shows the highest overall removal efficiency, achieving nearly complete removal through combined adsorption and Fenton-like degradation. These differences suggest variations in catalytic activity and potential radical scavenging effects at higher catalyst concentrations [49]. As the reaction progresses, all curves eventually become parallel, indicating that the system has attained its maximum removal efficiency.

### 2.2.4. Effect of pH

Figure 8 shows the variation in Rh-B removal efficiency at different pH levels. In the initial phase, adsorption occurs at all pH values (3, 5, 7, and 9), accompanied by a rapid increase in removal efficiency. Due to the number of unoccupied active sites on the nanocomposite surface, removal efficiency improved quickly during the adsorption phase at all measured pH values, reaching 52% at pH 3, 44% at pH 5, 45% at pH 7, and 39% at pH 9 after 60 min. The adsorption curves converge toward identical values, given their minor differences, suggesting that pH has only a moderate impact on the initial adsorption capacity [50]. Upon the addition of $H_2O_2$, the system entered the Fenton degradation phase, where pH had a stronger effect. The maximum degradation efficiency, 99.39%, was observed at pH 3, consistent with the Fenton reaction being most effective in moderately

acidic conditions. This indicates that acidic conditions favor $H_2O_2$ activation and the generation of reactive oxygen species, leading to more efficient Rh-B degradation. In contrast, neutral and alkaline conditions reduce the Fenton-like degradation efficiency, likely due to less effective $H_2O_2$ activation and weaker interaction between Rh-B molecules and catalytic active sites.

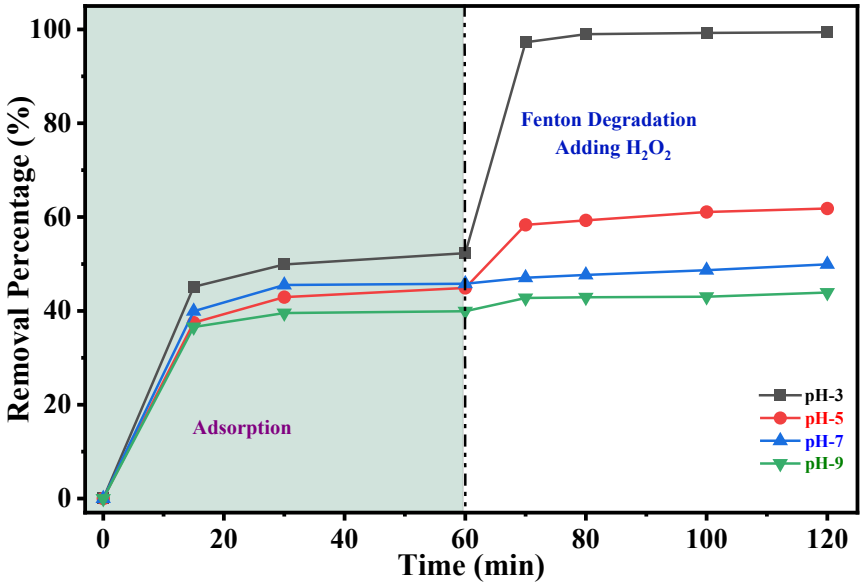


**Figure 8.** Effect of pH on the removal efficiency of Rh-B using A-ATP/NiO.

Degradation efficiencies were 61% and 49% at pH 5 and 7, respectively, demonstrating that neutral circumstances somewhat limit the process but do not completely inhibit it [51]. The efficiency decreased slightly to 43% at pH 9, which is explained by the lower activation of $H_2O_2$ by NiO during the degradation process, leading to lower generation of reactive oxygen species. This indicates that alkaline conditions inhibit the Fenton reaction, most likely by reducing hydroxyl radical formation. Furthermore, under alkaline conditions, the catalyst surface charge may change, decreasing the interaction between Rh-B molecules and the active catalytic sites and, thus, the degradation efficiency [52]. However, the findings show that Fenton degradation is highly pH-dependent, working best in acidic environments, whereas the A-ATP/NiO nanocomposite exhibits robust adsorption across all tested pH values [53].

### 2.2.5. Effect of $H_2O_2$ Concentration

Figure 9 shows the impact of various $H_2O_2$ concentrations (2, 4, and 5 mmol $L^{-1}$) on Rh-B removal efficiency using A-ATP/NiO. All three concentrations exhibit almost similar trends during adsorption: an initial steep increase in removal efficiency, followed by a smooth leveling off [54]. The comparable adsorption behavior observed before Fenton addition suggests that pollutant uptake was mainly governed by the availability of sufficient active sites on the material surface, resulting in only slight variations among the tested systems. After $H_2O_2$ addition, Rh-B degradation increased rapidly at all tested Fenton concentrations; however, the degradation efficiency was concentration-dependent. The 2 mmol $L^{-1}$ system showed comparatively lower degradation, reaching about 94%, whereas the 4 and 5 mmol $L^{-1}$ systems achieved nearly complete degradation, up to 99% [55]. This improvement indicates that increasing the Fenton concentration from 2 to 4 mmol $L^{-1}$ enhanced the generation of oxidative radicals and promoted Rh-B degradation. However, the similar performance at 4 and 5 mmol $L^{-1}$ suggests that further increasing the concentration beyond 4 mmol $L^{-1}$ did not yield a significant additional improvement,

indicating that 4 mmol $L^{-1}$ may be sufficient to achieve maximum degradation efficiency under the tested conditions [56]. Overall, $H_2O_2$ concentration showed a limited effect after 4 mmol $L^{-1}$. The increase from 2 to 4 mmol $L^{-1}$ improved Rh-B degradation, indicating enhanced reactive oxygen species generation. However, similar efficiencies at 4 and 5 mmol $L^{-1}$ suggest that the reaction reached near-saturation, and that further $H_2O_2$ addition did not significantly improve degradation under the studied conditions.

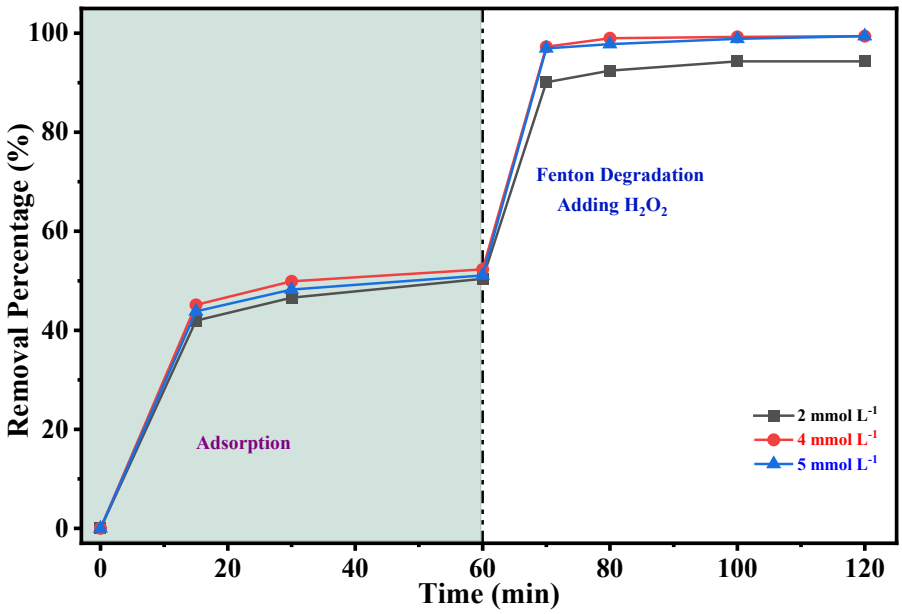


**Figure 9.** Influence of $H_2O_2$ concentration (2, 4, and 5 mmol $L^{-1}$) on the removal efficiency of Rh-B using A-ATP/NiO.

### 2.2.6. Impact of Dye

The impact of dye concentration on Rh-B removal using the A-ATP/NiO nanocomposite is shown in Figure 10. As the dye molecules adsorb onto the catalyst surface, the removal efficiency increases. During the first 15 min of adsorption, removal efficiencies of 54%, 49%, 45%, and 25% were achieved for 20, 30, 50, and 100 ppm Rh-B, respectively, due to the availability of abundant vacant active sites and a strong concentration gradient. The adsorption rate then gradually slowed and reached equilibrium at 65%, 59%, 52%, and 31%, indicating progressive occupation of surface active sites, particularly at higher dye concentrations [57]. Upon adding $H_2O_2$ to initiate the Fenton reaction, the removal efficiency increases significantly across all concentrations. After 120 min, the 20 ppm and 30 ppm solutions reach 100% degradation, the 50 ppm solution approaches 99.39%, and the 100 ppm solution exhibits 77% efficiency. Although the absolute ΔRP% between 60 and 120 min appears comparable, this parameter alone does not fully reflect the effect of initial dye concentration. The final removal efficiency shows a clear concentration-dependent trend: 20, 30, and 50 ppm achieved nearly complete Rh-B degradation, whereas 100 ppm showed lower removal efficiency. This is because at higher dye loadings, the fixed catalyst and $H_2O_2$ dosages generate fewer reactive oxygen species per dye molecule, thereby limiting Fenton-like degradation performance. These findings show that the Fenton reaction is highly effective, especially at modest dye concentrations [58]. The A-ATP/NiO nanocomposite exhibits robust adsorption and nearly full Fenton decomposition, demonstrating its efficacy for pollutant removal, and the 50 ppm solution shows an ideal balance among the measured concentrations.

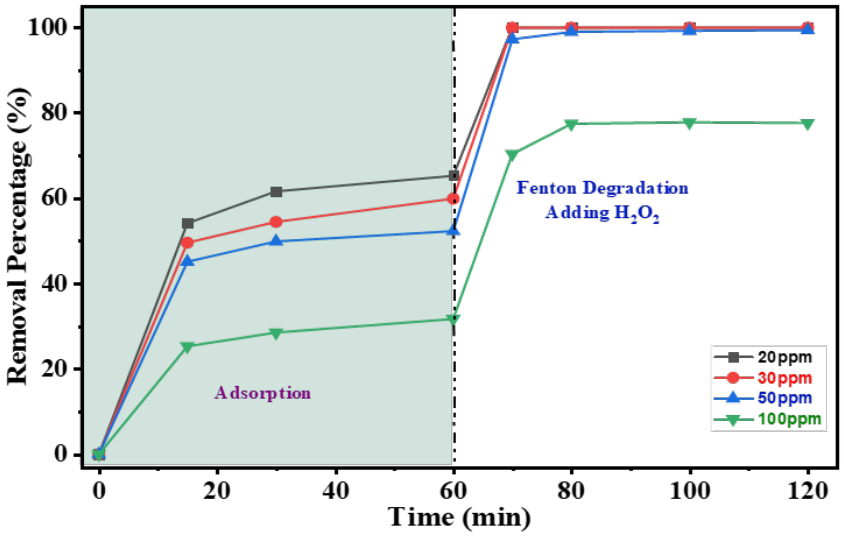


**Figure 10.** Influence of initial Rh-B concentration (20, 30, 50, and 100 ppm) on removal efficiency using A-ATP/NiO, showing faster and more complete removal at lower dye concentrations.

### *2.3. Oxidation Kinetics*

The Fenton-like oxidation kinetics were investigated using pseudo-first- and pseudo-second-order models.

$$\ln\left(\frac{C_t}{C_o}\right) = -k_{app}t \quad (2)$$

$$\frac{1}{C_t} - \frac{1}{C_o} = kt \quad (3)$$

The pseudo-first-order (PFO) kinetic behavior of Rh-B degradation across different catalysts is shown in Figure 11a. The linearity of the plots confirms that, for all catalysts, the degradation process obeys pseudo-first-order kinetics. The measured rate constants, represented by the slopes of these lines, show that NiO-supported ATP samples have greater reaction rates than unmodified R-ATP, P-ATP, and A-ATP. This indicates that NiO modification significantly enhances catalytic activity, thereby accelerating the oxidative degradation of Rh-B [59]. P-ATP/NiO has the fastest reaction rate, the steepest slope, and the best linearity ($R^2$ = 0.984) among the catalysts, suggesting that it fits the pseudo-first-order model very well. R-ATP has a modest fit ($R^2$ = 0.893), consistent with its lower catalytic activity, whereas P-ATP and A-ATP likewise closely match the model ($R^2$ = 0.950 and $R^2$= 0.956). A-ATP/NiO exhibits a good value ($R^2$ = 0.954), indicating slower radical-generation kinetics or more complicated reaction behavior. A comparative analysis of different adsorbents with Rh-B dye is summarized in Table 3.

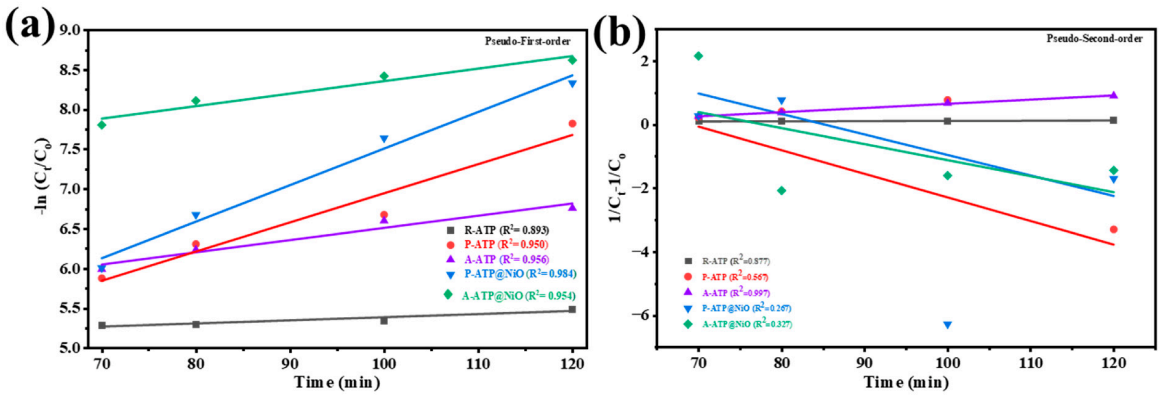


**Figure 11.** (**a**) Pseudo-first-order of R-ATP, P-ATP, A-ATP, P-ATP/NiO, and A-ATP/NiO. (**b**) Pseudo-second-order of R-ATP, P-ATP, A-ATP, P-ATP/NiO, and A-ATP/NiO.

Plotting $1/Ct - 1/Co$ as a function of time illustrates the pseudo-second-order (PSO) kinetic model shown in Figure 11b. A linear relationship in this case would suggest a second-order kinetic process. These curves exhibit erratic patterns with multiple upward and downward movements, in contrast to the first-order plot, suggesting a weaker adherence to second-order kinetics [60]. This discrepancy is supported by the $R^2$ values, with R-ATP ($R^2$ = 0.877) exhibiting the best, but still the poorest, fit compared to its first-order behavior. While NiO/A-ATP and NiO/P-ATP perform even worse ($R^2$ = 0.327 and 0.267, respectively), P-ATP has a low fit ($R^2$ = 0.567), and A-ATP follows both with a good fit. The sharp, non-linear variations, particularly the significant negative dips for P-ATP/NiO and A-ATP/NiO, suggest that these catalysts likely follow intricate radical-mediated mechanisms rather than second-order kinetics. Overall, Figure 11 confirms that pseudo-first-order kinetics is the more suitable model for explaining the Fenton-like degradation behavior, as the oxidation process does not follow pseudo-second-order kinetics for any catalyst.

**Table 3.** Comparative analysis of Rh-B dye with different adsorbents.

| Catalyst | Rh-B (mg/L) | Catalyst Dose (g/L) | $H_2O_2$ (mmol/L) | Degradation % | Mechanism | Ref. |
|---|---|---|---|---|---|---|
| $Cu/Al_2O_3/g\text{-}C_3N_4$ | 20 | 1.0 | 10 | 96.4% (100 min) | Fenton-like | [61] |
| Magnetic Biochar (RBCF12) | 100 | 0.5 | 20 | 91.67% (120 min) | Fenton-like/Electro-Fenton | [62] |
| Nano-iron oxide/bentonite | 7.5 | 0.3 | 10 | 97% (240 min) | Heterogeneous photo-Fenton | [63] |
| $Fe_3Cu_2$/HZSM-5 | 20 | 3.0 | 5.3 | ~100% (100 min) | Fenton-like | [64] |
| A-ATP/NiO | 50 | 0.03 | 5 | 99.39% (120 min) | Adsorption + Fenton-like | This work |

### *2.4. Degradation Mechanism*

In the A-ATP/NiO system, the removal of Rh-B is governed by improved adsorption on the nanocomposite surface, followed by Fenton-like oxidation of the remaining dye after $H_2O_2$ addition [7], as shown in Figure 12. During the initial dark adsorption stage, Rh-B molecules are enriched on the composite surface through diffusion into the porous attapulgite network, interaction with surface hydroxyl groups, and adsorption onto the activated clay nanocomposite [14]. The fibrous ATP matrix not only provides high-accessibility support for pollutant (Rh-B) uptake but also promotes uniform dispersion of NiO nanoparticles, thereby maximizing contact among the adsorbed dye, the oxidant, and the catalytic sites [65]. This preconcentration step is reflected in the 52% Rh-B removal achieved within 60 min before $H_2O_2$ addition. After $H_2O_2$ is introduced, the supported NiO phase activates hydrogen peroxide through a surface $Ni^{2+}/Ni^{3+}$ redox cycle, generating highly reactive oxygen species, predominantly hydroxyl radicals (•OH), with possible contribution from secondary species such as $HO_2\bullet/O_2^{-}\bullet$. This interpretation is also supported by recent reports showing that NiO-based metal oxide systems can promote the generation of hydroxyl radicals and other reactive oxygen species, thereby facilitating the oxidative degradation of organic contaminants [66]. Because Rh-B has already been concentrated near the catalytic interface, these reactive species can rapidly attack the dye molecules adsorbed on or near the catalyst surface, leading to a sharp increase in removal from 52% to 99.39% within 120 min. The oxidation of Rh-B is expected to proceed through successive N-de-ethylation, cleavage of the xanthene chromophore, opening of aromatic structures, and further conversion of low-molecular-weight intermediates into simpler end products [67]. Thus, activated attapulgite serves a dual role as both an adsorptive platform and a catalyst support. At the same time, NiO functions as the primary Fenton-like active phase for $H_2O_2$ decomposition

and radical generation. This synergistic interaction enables efficient interfacial degradation of Rh-B. Consequently, the overall performance of the A-ATP/NiO system arises from the cooperative interplay between pollutant enrichment through adsorption and rapid surface oxidation driven by Fenton-like catalysis [68].

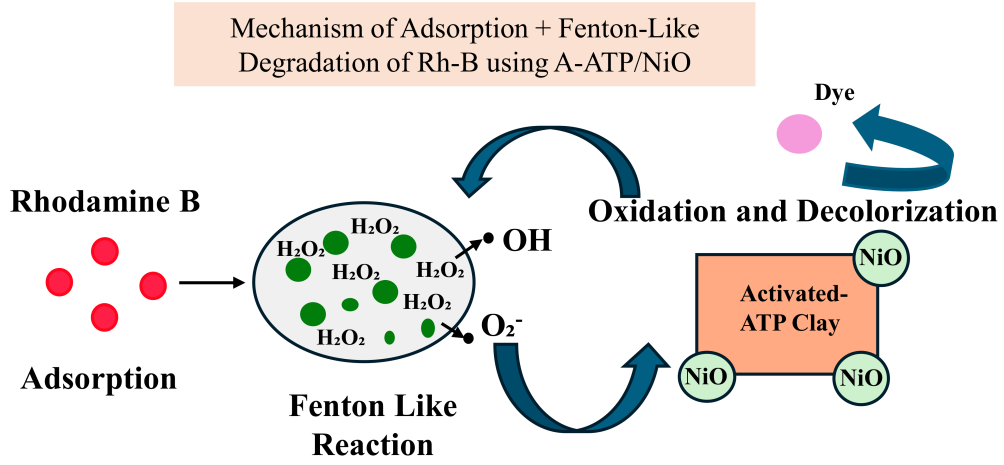


**Figure 12.** Adsorption and Fenton-like degradation mechanism of Rh-B dye removal.

Reactive oxygen species (ROS) generated through $H_2O_2$ activation on the catalyst surface are responsible for Rh-B degradation. Previous studies have demonstrated that heterogeneous Fenton-like systems can generate multiple ROS, including hydroxyl radicals (•OH), which collectively contribute to pollutant oxidation. As shown in Figure 13, the role of hydroxyl radicals (•OH) in the A-ATP/NiO in $H_2O_2$ system was evaluated using tertiary butanol (TBA) as a •OH scavenger. In the absence of TBA, the system showed rapid Rh-B degradation, reaching 97% within 10 min and 99.39% after 60 min. However, the addition of TBA significantly reduced the degradation efficiency in a concentration-dependent manner. The degradation efficiency decreased from 99.39% to 75%, 68%, and 46% at TBA concentrations of 125, 167, and 500 mmol $L^{-1}$, respectively [7]. This progressive inhibition indicates that TBA competed with Rh-B for •OH radicals, thereby decreasing the availability of •OH radicals for Rh-B oxidation. Therefore, •OH radicals are considered the dominant reactive species in the A-ATP/NiO in the Fenton system [69]. A possible mechanism is that $H_2O_2$ is adsorbed and activated on the NiO-containing catalyst surface, where surface Ni active sites promote the generation of •OH radicals. These radicals then attack the Rh-B chromophore, leading to the dye's oxidative degradation. Since Rh-B degradation was not completely suppressed even at the highest TBA concentration, minor surface-mediated oxidation pathways may also contribute to the overall degradation process [70,71].

### *2.5. Reusability*

The reusability of A-ATP/NiO was evaluated for three consecutive Rh-B removal cycles (Figure 14). After each run, the composite was recovered by centrifugation, dried overnight, and reused under the same conditions. The adsorption efficiency decreased slightly from 35% in the first cycle to 29% and 27% in the second and third cycles, respectively. Meanwhile, the Fenton degradation efficiency remained high, decreasing only from 94% to 91% and 88% after three cycles. This slight reduction may be due to partial loss of active sites, residual dye intermediates on the catalyst surface, or minor material loss during recovery [14]. Overall, the results indicate that A-ATP/NiO has good reusability and maintains stable catalytic performance for Rh-B degradation.

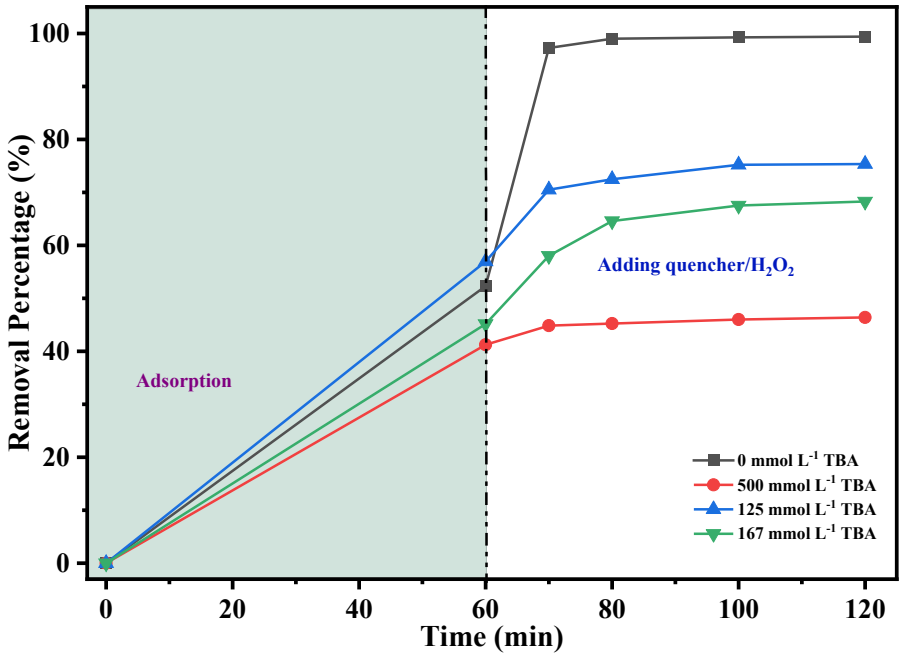


**Figure 13.** Effect of radical scavenger (TBA) concentration on Rh-B degradation in the A-ATP/NiO/$H_2O_2$ system, including the absence of a quencher.

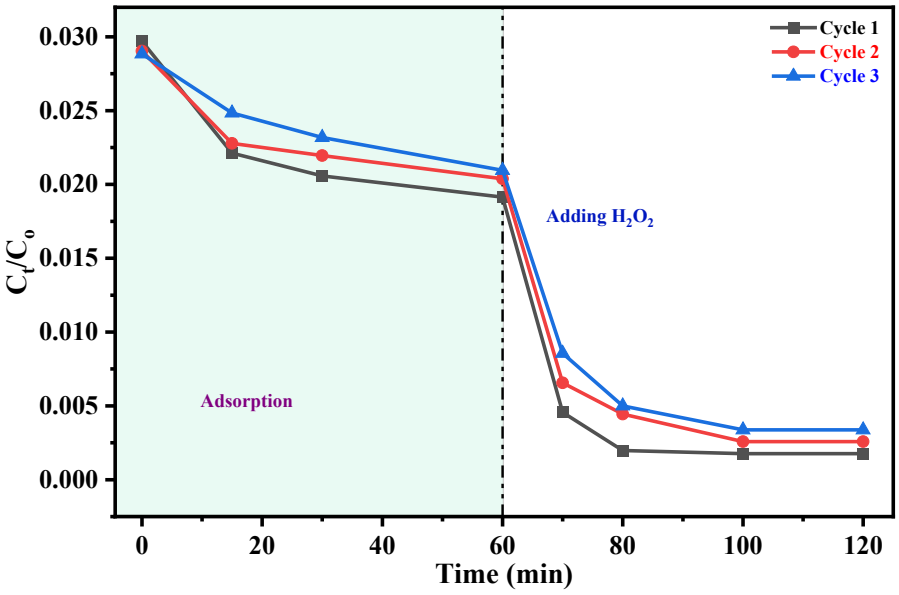


**Figure 14.** Reusability of A-ATP/NiO nanocomposite for Rhodamine B degradation.

## 3. Materials and Methods

### *3.1. Chemicals*

Nickel nitrate hexahydrate ($Ni(NO_3)_2 \cdot 6H_2O$ was purchased from Aladdin Bio-Chem Technology Co., Ltd. (Shanghai, China). Sodium hexametaphosphate (SHMP) was obtained from Fuchen Chemical Reagents Co., Ltd. (Tianjin, China). Natural attapulgite clay (R-ATP) was obtained from Gansu Western Attapulgite Research and Application Institute (Baiyin, China). All solutions were prepared using distilled water produced by a laboratory purification system. The reagents were of analytical grade and used as received without further purification.

### *3.2. Purification and Activation of Attapulgite (P-ATP)*

Purification of raw attapulgite (R-ATP) was carried out using a dispersant-assisted sedimentation and centrifugation method. First, 6 g of sodium hexametaphosphate (SHMP) was dissolved in 200 mL of distilled water under magnetic stirring until a homogeneous solution formed. Then, 20 g of R-ATP clay was slowly added to this solution and stirred mechanically for 1 h to ensure complete dispersion. To reduce particle aggregation, the suspension was passed through a colloid mill three times. After that, it was subjected to ultrasonic treatment for 2 h, with simultaneous mechanical stirring, to delaminate clay layers. After sonication, the suspension was allowed to settle for 1.5 h to facilitate the sedimentation of coarse particles. The colloidal supernatant was carefully separated and centrifuged at 3800 rpm for 30 min to isolate the fine fraction. For further refinement, a density gradient centrifugation was performed using sucrose solutions of varying concentrations (50%, 40%, 30%, and 20% *w*/*w*) layered in descending order of density. The clay suspension was gently placed on top of the gradient and centrifuged at 500 rpm for 45 min. The purified attapulgite fraction (P-ATP) was collected, oven-dried at 60 °C for 12 h, and ground to a fine powder for subsequent characterization and adsorption and degradation experiments. For activation, 1 g of P-ATP was added to 200 mL of 1 M HCl and stirred for 5 h. The mixture was then centrifuged, and the resulting solid was dried to obtain the activated attapulgite (A-ATP), which was used in subsequent adsorption and Fenton-like degradation experiments.

### *3.3. Synthesis of A-ATP/NiO Nanocomposite*

The NiO/attapulgite nanocomposite (P-ATP/NiO and A-ATP/NiO) was formed by dispersing 1 g of acid-activated clay into 50 mL of distilled water for 40 min. Separately, 0.5 g of $Ni(NO_3)_2 \cdot 6H_2O$ was dissolved in 50 mL of distilled water and added to the clay suspension, which was then stirred for 1 h. To achieve a pH of 12, 0.3 M (NaOH) solution was added, and the suspension was stirred for an additional 40 min. The solid product was separated by centrifugation, washed thoroughly with deionized water to remove residual nickel ions, dried at 70 °C overnight, and calcined at 500 °C for 3 h. The final product was collected and stored for further use. The schematic diagram in Figure 15 outlines the synthesis steps for forming the nanocomposite.

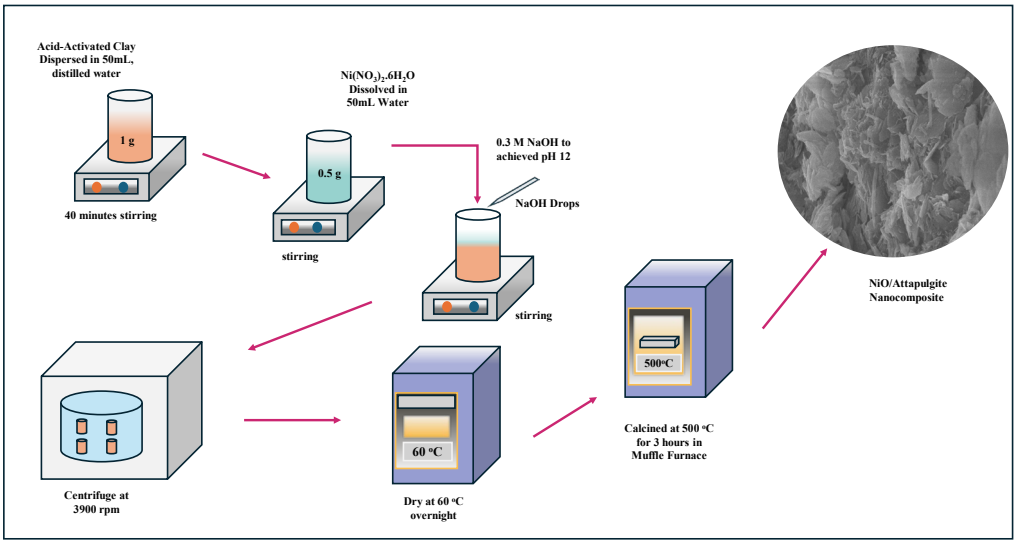


**Figure 15.** Schematic diagram for the formation of A-ATP/NiO nanocomposite.

### *3.4. Characterization*

The surface morphology of R-ATP, P-ATP, and NiO-modified attapulgite (P-ATP/NiO and A-ATP/NiO) nanocomposites was examined using a Scanning Electron Microscope (SEM, Supra 55, Zeiss, Oberkochen, Germany). The phase structure and crystallinity of the samples were analyzed using X-ray Diffraction (XRD, XRD-6000, Shimadzu, Kyoto, Japan) with a scanning rate of $10^\circ$ $min^{-1}$ over 3–$70^\circ/2\theta$. The surface area and pore volume were evaluated by $N_2$ adsorption–desorption analysis using a Quantachrome Chrome 3QDS-MP-30 analyser (Quantachrome, Boynton Beach, FL, USA) and calculated using the Brunauer–Emmett–Teller (BET) method. Functional groups present in R-ATP, P-ATP, and composite samples were identified using a Fourier Transform Infrared Spectrometer (FTIR, TENSOR II, Bruker, Germany). The Rh-B dye concentration during adsorption and degradation experiments was quantified using a UV–visible spectrophotometer (UV-2501PC, Shimadzu, Japan) at $\lambda$ = 554 nm.

### *3.5. Batch Experiments*

Batch adsorption and degradation experiments were performed using a 50 ppm Rh-B stock solution. For each experiment, 100 mL of the dye solution was placed in a 250 mL conical flask. Subsequently, 30 mg (0.03 g $L^{-1}$) of the prepared adsorbent (A-ATP/NiO) was added to the solution and placed on a thermostatic orbital shaker at 180 rpm for 60 min in the dark. After that, $H_2O_2$ was introduced to initiate the Fenton-like degradation process. The experiments were also conducted to determine the effect of pH (3–9), the effect of catalyst dose (0.01–0.03 g $L^{-1}$), the effect of time (0–120 min), the effect of temperature (303 K–333 K), effect of $H_2O_2$ amount (4–30 mmol $L^{-1}$), and the effect of dye concentration (20 ppm–100 ppm). Samples (2 mL) were withdrawn at predetermined intervals (t = 0, 15, 30, and 60 min) using a syringe and filtered for UV–vis analysis to determine the remaining Rh-B concentration during the experiment. After 60 min of adsorption, hydrogen peroxide ($H_2O_2$) was added to initiate Fenton-like degradation. Additional samples were collected at t = 70, 80, 100, and 120 min to monitor the rate of dye degradation. The total experiment time was 120 min, consisting of 1 h of adsorption followed by 1 h of degradation. After completion, the remaining solution was centrifuged to recover the adsorbent, which was washed and stored for further use. The dye removal efficiency was calculated according to Equation (4):

$$R\ (\%) = (C_0 - C_t)/C_0 \times 100 \quad (4)$$

where $C_0$ and $C_t$ (mg $L^{-1}$) represent the initial and residual dye concentrations at time t, respectively.

## 4. Conclusions

A natural R-ATP was purified to obtain P-ATP, followed by acid activation to produce A-ATP. Nickel oxide was then impregnated into the activated clay to synthesize the A-ATP/NiO composite. This material was used for Rh-B removal via improved adsorption, followed by Fenton-like degradation upon $H_2O_2$ addition. After $H_2O_2$ addition, A-ATP/NiO achieved a total degradation removal rate of 99.39%. The highest removal efficiency was observed at pH 3. At 303 K, the catalyst achieved almost complete Rh-B degradation. The optimal catalyst dosage (A-ATP/NiO) was 0.03 g $L^{-1}$, and the initial dye concentration was 50 ppm. Adsorption alone removed 52% of the Rh-B dye, and with the addition of 5 mmol $L^{-1}$ $H_2O_2$, the degradation reached its maximum value (99.39%). Kinetic analysis confirmed that the removal process followed a pseudo-first-order model. The results demonstrate that the cooperative interaction between nickel oxide and hydrogen peroxide promotes the possible formation of highly reactive radicals, including hydroxyl (OH•) and superoxide ($O_2^-$•), which are responsible for the effective breakdown of Rh-B

dye molecules. Overall, this work offers a novel strategy for upgrading low-grade ATP into a high-performance catalytic material. The A-ATP/NiO nanocomposite, based on an improved adsorption and Fenton-like oxidation approach, provides a cost-effective and environmentally friendly pathway for designing wastewater treatment materials.

**Author Contributions:** Methodology, investigation, and writing—original draft preparation, S.A. (Sadiq Ali); conceptualization and writing—review and editing, S.A. (Saeed Ahmed), H.L. and Y.F.; supervision, Y.F. All authors have read and agreed to the published version of the manuscript.

**Funding:** This research received no external funding.

**Data Availability Statement:** The original contributions presented in this study are included in the article. Further inquiries can be directed to the corresponding author.

**Acknowledgments:** Yongjun Feng acknowledges personal support from the Mount Tai Industrial Leading Talent Project. The attapulgite was generously donated by Gansu Cuihua Technology Co., Ltd. (H2020292).

**Conflicts of Interest:** The authors declare no conflict of interest.

## References

1. Liu, Y.; Chen, J.; Duan, D.; Zhang, Z.; Liu, C.; Cai, W.; Zhao, Z. Environmental impacts and biological technologies toward sustainable treatment of textile dyeing wastewater: A review. *Sustainability* **2024**, *16*, 10876. [CrossRef]
2. Dutta, S.; Adhikary, S.; Bhattacharya, S.; Roy, D.; Chatterjee, S.; Chakraborty, A.; Banerjee, D.; Ganguly, A.; Nanda, S.; Rajak, P. Contamination of textile dyes in aquatic environment: Adverse impacts on aquatic ecosystem and human health, and its management using bioremediation. *J. Environ. Manag.* **2024**, *353*, 120103. [CrossRef]
3. Islam, M.T.; Islam, T.; Islam, T.; Repon, M.R. Synthetic dyes for textile colouration: Process, factors and environmental impact. *Text. Leather Rev.* **2022**, *5*, 327–373. [CrossRef]
4. Kolya, H.; Kang, C.-W. Toxicity of metal oxides, dyes, and dissolved organic matter in water: Implications for the environment and human health. *Toxics* **2024**, *12*, 111. [CrossRef] [PubMed]
5. Sonone, S.S.; Jadhav, S.; Sankhla, M.S.; Kumar, R. Water contamination by heavy metals and their toxic effect on aquaculture and human health through food Chain. *Lett. Appl. NanoBioScience* **2020**, *10*, 2148–2166. [CrossRef]
6. El-Ghobashy, M.A.; Hashim, H.; Darwish, M.A.; Khandaker, M.U.; Sulieman, A.; Tamam, N.; Trukhanov, S.V.; Trukhanov, A.V.; Salem, M.A. Eco-friendly NiO/polydopamine nanocomposite for efficient removal of dyes from wastewater. *Nanomaterials* **2022**, *12*, 1103. [CrossRef] [PubMed]
7. Jiang, C.; Liu, X.; Wang, X.; Wang, Q.; Li, H.; Tian, W.; Ahmed, S.; Feng, Y. Coupling adsorption and in-situ Fenton-like oxidation by iron-containing low-grade attapulgite clay towards organic pollutant removal: From batch experiment to continuous operation. *Green Energy Environ.* **2025**, *10*, 1015–1026. [CrossRef]
8. Zhang, T.; Huang, X.; Qiao, J.; Liu, Y.; Zhang, J.; Wang, Y. Recent developments in synthesis of attapulgite composite materials for refractory organic wastewater treatment: A review. *RSC Adv.* **2024**, *14*, 16300–16317. [CrossRef] [PubMed]
9. Wang, Y.; Feng, Y.; Jiang, J.; Yao, J. Designing of recyclable attapulgite for wastewater treatments: A review. *ACS Sustain. Chem. Eng.* **2019**, *7*, 1855–1869. [CrossRef]
10. Li, H.J.; Xu, J.H.; Wang, L.Q.; Hou, D.D.; Wang, Z.R.; Li, H.Z. Adsorption properties of modified ATP-RGO composite aerogel for removal of malachite green and methyl orange from unitary and binary aqueous solutions. *Adsorpt. Sci. Technol.* **2022**, *2022*, 5455330. [CrossRef]
11. Rafique, M.A.; Kiran, S.; Javed, S.; Ahmad, I.; Yousaf, S.; Iqbal, N.; Afzal, G.; Rani, F. Green synthesis of nickel oxide nanoparticles using Allium cepa peels for degradation of congo red direct dye: An environmental remedial approach. *Water Sci. Technol.* **2021**, *84*, 2793–2804. [CrossRef] [PubMed]
12. Kiran, S.; Rafique, M.A.; Ashraf, A.; Farooq, T.; Iqbal, S.; Afzal, G.; Ajmal, S.; Naz, S. Green synthesis of nickel nanoparticles using fruit peels of citrus paradise for remediation of congo red dye. *J. Mex. Chem. Soc.* **2021**, *65*, 507–515. [CrossRef]
13. Sing, K.S. Reporting physisorption data for gas/solid systems with special reference to the determination of surface area and porosity (recommendations 1984). *Pure Appl. Chem.* **1985**, *57*, 603–619. [CrossRef]
14. Karim, N.; Kyawoo, T.; Jiang, C.; Ahmed, S.; Tian, W.; Li, H.; Feng, Y. Fenton-like degradation of methylene blue on attapulgite clay composite by loading of iron–oxide: Eco-friendly preparation and its catalytic activity. *Materials* **2024**, *17*, 2615. [CrossRef] [PubMed]

15. Lu, Y.; Zhang, H.; Wang, Q.; Wang, A. Hydrochloric acid pretreatment combined with microwave-assisted oxalic acid leaching of natural red palygorskite-rich clay for efficiently change the color and properties. *Appl. Clay Sci.* **2022**, *228*, 106594. [CrossRef]
16. Boudriche, L.; Calvet, R.; Hamdi, B.; Balard, H. Effect of acid treatment on surface properties evolution of attapulgite clay: An application of inverse gas chromatography. *Colloids Surf. A Physicochem. Eng. Asp.* **2011**, *392*, 45–54. [CrossRef]
17. Huo, C.; Yang, H. Attachment of nickel oxide nanoparticles on the surface of palygorskite nanofibers. *J. Colloid Interface Sci.* **2012**, *384*, 55–60. [CrossRef] [PubMed]
18. Zhang, L.-F.; Hu, Z.-P.; Liang, S.-H.; Xu, F.; Yuan, Z.-Y. Nickel nanoparticles anchored on activated attapulgite clay for ammonia decomposition to hydrogen. *Symmetry* **2022**, *14*, 2627. [CrossRef]
19. Karimi, H.; Heidari, M.A.; Emrooz, H.B.M.; Shokouhimehr, M. Carbonization temperature effects on adsorption performance of metal-organic framework derived nanoporous carbon for removal of methylene blue from wastewater; experimental and spectrometry study. *Diam. Relat. Mater.* **2020**, *108*, 107999. [CrossRef]
20. Mannaa, M.A.; Qasim, K.F.; Alshorifi, F.T.; El-Bahy, S.M.; Salama, R.S. Role of NiO nanoparticles in enhancing structure properties of $TiO_2$ and its applications in photodegradation and hydrogen evolution. *ACS Omega* **2021**, *6*, 30386–30400. [CrossRef] [PubMed]
21. Elfeky, S.A.; Mahmoud, S.E.; Youssef, A.F. Applications of CTAB modified magnetic nanoparticles for removal of chromium (VI) from contaminated water. *J. Adv. Res.* **2017**, *8*, 435–443. [CrossRef] [PubMed]
22. Liu, Y.; Chen, H.; Chai, L.; Liu, J.; Huang, S.; Liu, F.; Wei, M.; Zhu, X.; Zhang, Y.; Liu, M. A dual-channel sensing platform for ATP and copper ions via the target-induced peroxidase mimics activity and fluorescence variations of iron oxide nanoparticles-modified metal-organic frameworks. *Sens. Actuators B Chem.* **2024**, *418*, 136226. [CrossRef]
23. Quaroni, L.; Zlateva, T.; Normand, E. Detection of weak absorption changes from molecular events in time-resolved FT-IR spectromicroscopy measurements of single functional cells. *Anal. Chem.* **2011**, *83*, 7371–7380. [CrossRef] [PubMed]
24. Nasir, Z.; Ali, A.; Shakir, M.; Wahab, R. Silica-supported NiO nanocomposites prepared via a sol–gel technique and their excellent catalytic performance for one-pot multicomponent synthesis of benzodiazepine derivatives under microwave irradiation. *New J. Chem.* **2017**, *41*, 5893–5903. [CrossRef]
25. Fazlali, F.; Mahjoub, A.; Abazari, R. A new Route for Synthesis of Spherical NiO Nanoparticles via Emulsion Nano-Reactors With Enhanced Photocatalytic Activity. *Solid State Sci.* **2015**, *48*, 263–269. [CrossRef]
26. Yang, Z.; Xing, Z.; Yu, H.; Jin, G.; Yin, Y.; Song, Z.; Cui, X.; Zheng, W.; Gong, J.; Zhang, F. Tribological self-repairing behavior in ATP/Al composites: An orthogonal experimental study on attapulgite mineral effects. *J. Mater. Res. Technol.* **2025**, *37*, 2512–2527. [CrossRef]
27. Ma, G.; Meng, K.; Ren, J.; Tao, L.; Ding, J.; Dai, L.; Zhao, T.; Liao, C.; Zhou, Y.; Zhou, Y. Attapulgite-supported nanoscale zero-valent iron composite materials for the enhanced removal of $Ni^{2+}$ from aqueous solutions: Characterization, kinetics, and mechanism. *Appl. Sci.* **2024**, *14*, 1823. [CrossRef]
28. Anandan, K.; Rajendran, V. Morphological and size effects of NiO nanoparticles via solvothermal process and their optical properties. *Mater. Sci. Semicond. Process.* **2011**, *14*, 43–47. [CrossRef]
29. Maqsood, N.; Rimašauskas, M.; Ghobakhloo, M.; Mordas, G.; Skotnicová, K. Additive manufacturing of continuous carbon fiber reinforced polymer composites using materials extrusion process. Mechanical properties, process parameters, fracture analysis, challenges, and future prospect. A review. *Adv. Compos. Hybrid Mater.* **2024**, *7*, 202. [CrossRef]
30. Preda, I.; Mossanek, R.J.O.; Abbate, M.; Alvarez, L.; Méndez, J.; Gutiérrez, A.; Soriano, L. Surface contributions to the XPS spectra of nanostructured NiO deposited on HOPG. *Surf. Sci.* **2012**, *606*, 1426–1430. [CrossRef]
31. Wang, X.; Jiang, C.; Li, H.; Tian, W.; Ahmed, S.; Feng, Y. Colloid mill-assisted ultrasonic-fractional centrifugal purification of low-grade attapulgite and its modification for adsorption of congo red. *Materials* **2024**, *17*, 2034. [CrossRef] [PubMed]
32. Thimmegowda, D.Y.; Hindi, J.; Markunti, G.B.; Kakunje, M. Enhancement of mechanical properties of natural fiber reinforced polymer composites using different approaches—A review. *J. Compos. Sci.* **2025**, *9*, 220. [CrossRef]
33. Li, M.; Li, A.; Xu, H.; Feng, L. Fabrication of NiO/palygorskite Composite and Its Pseudocapacitance Performances. *Int. J. Electrochem. Sci.* **2015**, *10*, 4405–4415. [CrossRef]
34. Ding, X.; Wang, T.; Fu, Q.; Xu, Q.; Luo, Z.; Wang, K.; Wei, T.; Wang, Y.; Zhang, Y.; Ma, M. A novel haul road dust suppression system using de-alkalized red mud as road base material and ancillary palygorskite-based biopolymer surfactant. *Constr. Build. Mater.* **2025**, *494*, 143566. [CrossRef]
35. Khan, S.; Ajmal, S.; Hussain, T.; Rahman, M.U. Clay-based materials for enhanced water treatment: Adsorption mechanisms, challenges, and future directions. *J. Umm AL-Qura Univ. Appl. Sci.* **2025**, *11*, 219–234.
36. Kyawoo, T.; Wei, T.; Karim, N.; Jiang, C.; Ahmed, S.; Li, H. Magnesium silicate honeycomb structure on attapulgite clay composite by self-template method for adsorption of methylene blue. *Materials* **2025**, *18*, 792. [CrossRef] [PubMed]
37. Liu, D.; Wang, X.; Nie, L.; Zhang, B.; Zhou, J.; Liu, H.; Wang, W. Nickel distribution in soils and its relationship with lithology, mineralization and geochemical landscape across mainland China. *Ore Geol. Rev.* **2025**, *178*, 106476. [CrossRef]
38. Fang, Y.; Ni, X.; Xiao, Q.; Huang, S.; López-Valdivieso, A. Iron-based materials synthesized by mechanical ball milling for environmental contaminants removal: Progress and prospects. *Int. J. Environ. Res.* **2025**, *19*, 12.

39. Alexandre-Franco, M.F.; Rodríguez-Rasero, C.; González-Trejo, A.; Casas-Pulido, M.; Fernández-González, C.; Cuerda-Correa, E.M. Leveraging the potential of in situ green-synthesized zero-valent iron nanoparticles (NZVI) for advanced oxidation of clinical dyes in water. *Appl. Sci.* **2024**, *14*, 6558. [CrossRef]
40. Song, J.; Zhu, L.; Yu, S.; Li, G.; Wang, D. The synergistic effect of adsorption and Fenton oxidation for organic pollutants in water remediation: An overview. *RSC Adv.* **2024**, *14*, 33489–33511. [CrossRef] [PubMed]
41. Liang, L.; Cheng, L.; Zhang, Y.; Wang, Q.; Wu, Q.; Xue, Y.; Meng, X. Efficiency and mechanisms of rhodamine B degradation in Fenton-like systems based on zero-valent iron. *RSC Adv.* **2020**, *10*, 28509–28515. [CrossRef] [PubMed]
42. Wang, R.-Y.; Zhong, J.-P.; Li, Y.-Q.; Li, D.-X.; Meng, J.-Z.; Ding, K.-B.; Li, C.-H.; Liu, Z.-Q. Engineering amorphous/crystalline Ni/NiO electrocatalysts for highly efficient hydrogen peroxide production. *ACS Nano* **2025**, *19*, 38086–38096. [CrossRef] [PubMed]
43. Thanapornsin, W.; Pasee, K.; Puchongkawarin, C.; Umpuch, C. Preparation and characterization of biocomposite film made of activated carbon derived from microalgal biomass: An experimental design approach for basic yellow 1 removal. *South Afr. J. Chem. Eng.* **2024**, *47*, 178–196. [CrossRef]
44. Chen, H.; Pan, Y.; Zhang, W.; Long, A.; Chen, M.; Xiao, X.; Wang, Z.; Tang, M.; Peng, Y.; Sun, S. Adsorption-desorption of copper (II) by temperature-sensitive nano-biochar@ PNIPAM/alginate double-network composite hydrogel: Enhanced mechanisms and application potentials. *Chem. Eng. J.* **2024**, *495*, 153356. [CrossRef]
45. Liu, S.; Jassby, D.; Schäfer, A.I. Removal of steroid hormone micropollutants by an electrochemical carbon nanotube membrane flow-through reactor: Role of concentration and degradation mechanisms. *Adv. Funct. Mater.* **2026**, *36*, e10813.
46. Huang, W.; Gao, X.; Sun, L.; Chen, H.; Shan, P.; Shen, Y.; Zhang, S.; Wang, L.; Lu, C.; Shi, W. Black g-$C_3N_4$-based hydrogel for water evaporation and photothermal persulfate activation. *J. Mater. Sci. Technol.* **2026**, *249*, 153–163. [CrossRef]
47. Hussein, S.A.; Taha, G.M.; Adam, F.; Moghazy, M.A. Three different methods for ZnO-RGO nanocomposite synthesis and its adsorption capacity for methylene blue dye removal in a comparative study. *BMC Chem.* **2025**, *19*, 18. [CrossRef] [PubMed]
48. Jin, Z.; Xiao, S.; Dong, H.; Xiao, J.; Tian, R.; Chen, J.; Li, Y.; Li, L. Adsorption and catalytic degradation of organic contaminants by biochar: Overlooked role of biochar's particle size. *J. Hazard. Mater.* **2022**, *422*, 126928. [CrossRef] [PubMed]
49. Canillas, M.; Chinarro, E.; Freitas, M.; Pêgo, A.P.; Moreno, B. Titanium dioxide catalytic activity contributes to the process of free radical scavenging. *J. Catal.* **2020**, *381*, 186–192. [CrossRef]
50. Abid, L.H.; Mussa, Z.H.; Al-Qaim, F.F.; Kamyab, H.; Al-Saedi, H.F.S.; Kadhim, N.J.; Deyab, I.F.; Imran, A.F.; Al-Asadi, S.T. Application of $ZnCl_2$-modified biowaste to the removal of highly polluted dye: A case study of investigating the kinetics and adsorption isotherms. *Energy Nexus* **2025**, *19*, 100481. [CrossRef]
51. Sciscenko, I.; Vione, D.; Minella, M. Infancy of peracetic acid activation by iron, a new Fenton-based process: A review. *Heliyon* **2024**, *10*, e27036. [CrossRef] [PubMed]
52. Li, N.; He, X.; Ye, J.; Dai, H.; Peng, W.; Cheng, Z.; Yan, B.; Chen, G.; Wang, S. $H_2O_2$ activation and contaminants removal in heterogeneous Fenton-like systems. *J. Hazard. Mater.* **2023**, *458*, 131926. [CrossRef] [PubMed]
53. Chen, L.; Zhao, B.; Yang, M. Oxytetracycline degradation in water by $H_2O_2$: The effect of iron-loaded attapulgite calcination temperature. *Desalin. Water Treat.* **2025**, *324*, 101559. [CrossRef]
54. Jung, D.E.; Einck, V.J.; Dawicki, A.; Malgras, V.; Verrastro, L.D.; Grosso, D.; Arbabi, A.; Watkins, J.J. Full wafer scale manufacturing of directly printed $TiO_2$ metalenses at visible wavelengths with outstanding focusing efficiencies. *Adv. Mater.* **2025**, *37*, 2500327. [CrossRef] [PubMed]
55. Lu, C.; Hu, C.; Wu, J.; Rong, H.; Lyu, L. Endogenous substances utilization for water self-purification amplification driven by nonexpendable $H_2O_2$ over a micro-potential difference surface. *Environ. Sci. Technol.* **2024**, *58*, 23241–23250. [CrossRef] [PubMed]
56. Zheng, J.; Li, W.; Liu, X.; Hou, N.; Wang, Y.; Mu, Y. Localized surface plasmon resonance effect for superior Fenton-like catalysis. *Environ. Sci. Technol.* **2025**, *59*, 18979–18989. [CrossRef] [PubMed]
57. Sudarsan, S.; Murugesan, G.; Varadavenkatesan, T.; Vinayagam, R.; Selvaraj, R. Efficient adsorptive removal of congo red dye using activated carbon derived from spathodea campanulata flowers. *Sci. Rep.* **2025**, *15*, 1831. [CrossRef] [PubMed]
58. Nguyen, T.; Vu Xuan, M.; Kuznetsova, T.; Pham, L.; Kapysh, L.; Ivanets, A.; Le, T.; Bui, V.; Nguyen, H.; Doan, V.-D. Advanced $Mn_3O_4$/$Fe_3O_4$-carbon molecular sieve composite: A robust catalyst for heterogeneous photo-Fenton oxidation of organic dyes. *J. Porous Mater.* **2025**, *32*, 821–841. [CrossRef]
59. Truong, T.T.; Pham, T.T.; Truong, T.T.T.; Pham, T.D. Synthesis, characterization of novel ZnO/CuO nanoparticles, and the applications in photocatalytic performance for Rhodamine B dye degradation. *Environ. Sci. Pollut. Res.* **2022**, *29*, 22576–22588. [CrossRef] [PubMed]
60. Safa, M.B.; Steffy, J.P.; Syed, A.; Subhiksha, V.; Elgorban, A.M.; Verma, M.; Wong, L.S.; Khan, S.S. Unveiling the enhanced Rhodamine B degradation in water by $Sn_3O_4$@Au: Insight into degradation pathway and by-products toxicity evaluation. *J. Water Process Eng.* **2025**, *72*, 107475. [CrossRef]
61. Zhou, C.; Liu, Z.; Fang, L.; Guo, Y.; Feng, Y.; Yang, M. Kinetic and mechanistic study of Rhodamine B degradation by $H_2O_2$ and Cu/$Al_2O_3$/g-$C_3N_4$ composite. *Catalysts* **2020**, *10*, 317. [CrossRef]

62. Nguyen, M.L.; Nguyen, T.T.; Ngo, H.L. Efficient Rhodamine B degradation via Fenton-like and E-Fenton processes using magnetic biochar from rubber seed shells. *RSC Adv.* **2025**, *15*, 11327–11336. [CrossRef] [PubMed]
63. Liu, Y.; Li, Y.; Wen, L.; Hou, K.; Li, H. Synthesis, characterization and photo degradation application for dye-Rhodamine B of nano-iron oxide/bentonite. *Guang Pu Xue Yu Guang Pu Fen Xi* **2006**, *26*, 1939–1942. [PubMed]
64. Lu, J.-F.; Wang, H.; Zhou, Y.; Mao, X.-Y.; Feng, X.-Q.; Wang, S.; Zhao, Y.-H. Degradation of Rhodamine B by Fenton-like system with Fe-Cu/HZSM-5 catalyst. *J. Taiwan Inst. Chem. Eng.* **2026**, *178*, 106412. [CrossRef]
65. Han, X.; Gou, L.; Tang, S.; Cheng, F.; Zhang, M.; Guo, M. Enhanced heterogeneous Fenton-like degradation of refractory organic contaminants over Cu doped (Mg,Ni)(Fe,Al)$_2$O$_4$ synthesized from laterite nickel ore. *J. Environ. Manag.* **2021**, *283*, 111941. [CrossRef] [PubMed]
66. Haider, Z.; Ju, H. Strategies to Boost Photocatalytic Degradation of Emerging Contaminants Using ZnO Heterostructure Photocatalysts. *Appl. Sci.* **2026**, *16*, 5279. [CrossRef]
67. Xu, Y.; Guo, J.; Chen, X.; Shi, X.; Wen, S. Degradation of tannic acid in heterogeneous Fenton system and persulfate system using iron(III) modified attapulgite: Influencing factors and degradation mechanism analysis. *Desalin. Water Treat.* **2024**, *317*, 100160. [CrossRef]
68. Khan, Z.U.H.; Gul, N.S.; Sabahat, S.; Sun, J.; Tahir, K.; Shah, N.S.; Muhammad, N.; Rahim, A.; Imran, M.; Iqbal, J.; et al. Removal of organic pollutants through hydroxyl radical-based advanced oxidation processes. *Ecotoxicol. Environ. Saf.* **2023**, *267*, 115564. [CrossRef] [PubMed]
69. Zhou, P.; Dai, Z.; Lu, T.; Ru, X.; Ofori, M.A.; Yang, W.; Hou, J.; Jin, H. Degradation of Rhodamine B in Wastewater by Iron-Loaded Attapulgite Particle Heterogeneous Fenton Catalyst. *Catalysts* **2022**, *12*, 669. [CrossRef]
70. Ahmed, Y.; Zhong, J.; Yuan, Z.; Guo, J. Roles of reactive oxygen species in antibiotic resistant bacteria inactivation and micropollutant degradation in Fenton and photo-Fenton processes. *J. Hazard. Mater.* **2022**, *430*, 128408. [CrossRef] [PubMed]
71. Yi, Q.; Ji, J.; Shen, B.; Dong, C.; Liu, J.; Zhang, J.; Xing, M. Singlet Oxygen Triggered by Superoxide Radicals in a Molybdenum Cocatalytic Fenton Reaction with Enhanced REDOX Activity in the Environment. *Environ. Sci. Technol.* **2019**, *53*, 9725–9733. [CrossRef] [PubMed]